Feasibility of a Passive Collision Avoidance System (PCAS) Based on Staring Infrared Sensors

January 1998

E.H. Takken, E.J. Stone, R.G. Priest, J.C. Kershenstein
Naval Research Laboratory
Washington, DC 20375

ABSTRACT

This report finds that a light weight, passive collision avoidance (PCAS) system based on uncooled LWIR sensors is feasible for Hunter/Predator class UAVs. The candidate PCAS system is analyzed using a statistical measure based on warning time provided. Typically warning times of 10s of seconds could be provided with very low probability of missed detection due to encounters with light aircraft under contrast reversal conditions.

1.0 Introduction and Summary:

In this study, infrared technology is evaluated for the possible role of providing collision avoidance warning to operators of Hunter/Predator class unmanned air vehicles (UAV's). These vehicles carry 200 and 450 lb payloads, respectively, and typically fly covertly at an altitude of 15,000 feet.[1] However, they are also required to maintain surveillance operations by flying below the cloud ceiling when needed. At 3,000 feet increasing numbers of small, non-instrumented, non-radiating civilian aircraft present a collision hazard, and there is concern that some of these small craft may even operate at night without warning lights. There appears to be a growing need for a modest-range search and detection sensor system that is light enough to be carried on the UAV. The role of such a system is to provide the remote operator with a warning so that he can execute a collision avoidance maneuver.

Discussions with users of UAV's in the Department of Defense suggest that the performance design goal should be declaration of impending collision, day or night, with 80% confidence at 20 seconds warning time and with near-perfect 95% confidence if the warning time is only 10 seconds.

The main body of this report describes how warning time performance is modeled, and contains sections on contrast signature modeling, collision geometry, and detector performance. The baseline case is a Cessna 172 hazard aircraft flying at an altitude of 1 km in a midlatitude summer atmosphere. The effects on warning time of the hazard's speed, altitude, skin temperature, and atmosphere type are investigated. The probability space displays of the last section perhaps best illustrate the results. The following four plots summarize important cases. Individual points at (95%, 10 sec) and (80%, 20 sec) represent the suggested design goal.

Figure 1 shows that the desired performance can be achieved if eight uncooled LWIR subsensors are used, with those pointed forward having longer focal lengths than those pointing rearward. With this

REPORT DOCUMENTATION PAGE

Form Approved OMB No. 0704-0188

1. REPORT DATE (DD-MM-YYYY)	2. REPORT TYPE	3. DATES COVERED (FROM - TO)
01-01-1998	Conference Proceedings	xx-xx-1998 to xx-xx-1998

4. TITLE AND SUBTITLE
Feasibility of a Passive Collision Avoidance System (PCAS) Based on Staring Infrared Sensors
Unclassified

5a. CONTRACT NUMBER
5b. GRANT NUMBER
5c. PROGRAM ELEMENT NUMBER

6. AUTHOR(S)
Takken, E. H. ;
Stone, E. J. ;
Priest, R. G. ;
Kershenstein, J. C. ;

5d. PROJECT NUMBER
5e. TASK NUMBER
5f. WORK UNIT NUMBER

7. PERFORMING ORGANIZATION NAME AND ADDRESS
Naval Research Laboratory
Washington, DC20375

8. PERFORMING ORGANIZATION REPORT NUMBER

9. SPONSORING/MONITORING AGENCY NAME AND ADDRESS
Director, CECOM RDEC
Night Vision and electronic Sensors Directorate, Security Team
10221 Burbeck Road
Ft. Belvoir, VA22060-5806

10. SPONSOR/MONITOR'S ACRONYM(S)
11. SPONSOR/MONITOR'S REPORT NUMBER(S)

12. DISTRIBUTION/AVAILABILITY STATEMENT
APUBLIC RELEASE
,

13. SUPPLEMENTARY NOTES
See Also ADM201041, 1998 IRIS Proceedings on CD-ROM.

14. ABSTRACT
This report finds that a light weight, passive collision avoidance (PCAS) system based on uncooled LWIR sensors is feasible for Hunter/Predator class UAVs. The candidate PCAS system is analyzed using a statistical measure based on warning time provided. Typically warning times of 10s of seconds could be provided with very low probability of missed detection due to encounters with light aircraft under contrast reversal conditions.

15. SUBJECT TERMS

16. SECURITY CLASSIFICATION OF:			17. LIMITATION OF ABSTRACT	18. NUMBER OF PAGES	19. NAME OF RESPONSIBLE PERSON
a. REPORT	b. ABSTRACT	c. THIS PAGE	Public Release	20	Fenster, Lynn lfenster@dtic.mil
Unclassified	Unclassified	Unclassified			19b. TELEPHONE NUMBER International Area Code Area Code Telephone Number 703767-9007 DSN 427-9007

arrangement the total weight of the composite warning sensor would be close to ten pounds, the lenses contributing half of this total. Enhanced performance, better than the suggested requirement, can be achieved by increasing the number of subsensors and hence the total weight. With a dozen subsensors the total sensor weight would still be less than twenty pounds. As discussed more fully in the main text, total system cost, exclusive of real-time processor hardware cost, should be about $100,000.

Figure 1: Performance vs Number of Uncooled Subsensors

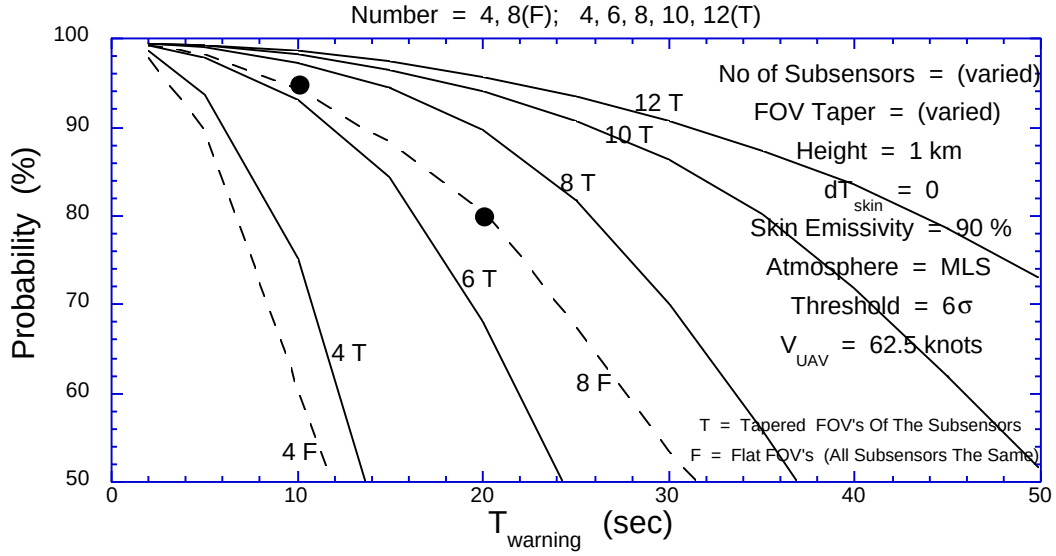

Figures 2 and 3 show the dependence of achievable warning time on flight altitude and on hazard skin heating or cooling. The infrared contrast signature of a Cessna 172 improves if the flight altitude is above or below 1 km. It is worst when the Cessna's skin temperature is slightly elevated (+2.5C), and better when the skin temperature is higher or lower than this due, for example, to solar heating or low emissivity.

In the infrared, an aircraft seen from below against a sky background usually appears as a warm object against the relatively cold sky (positive contrast), while an aircraft seen from above often appears cold against the relatively warm earth (negative contrast). Therefore, there is some position near the horizon where the contrast goes through zero, and the aircraft is undetectable.

Here contrast signature “improvement” means that these signature zero crossings occur at elevation look angles above or below the narrow, near-horizontal views from the UAV to the hazard aircraft. A pictorial representation of this is given in Section 5, based on details covered in Section 2.3. Figures 2 and 3 indicate that these zeros are most significant for 1 km altitude and for ambient-air skin temperature.

Figure 2: Effect Of Skin Warming & Cooling

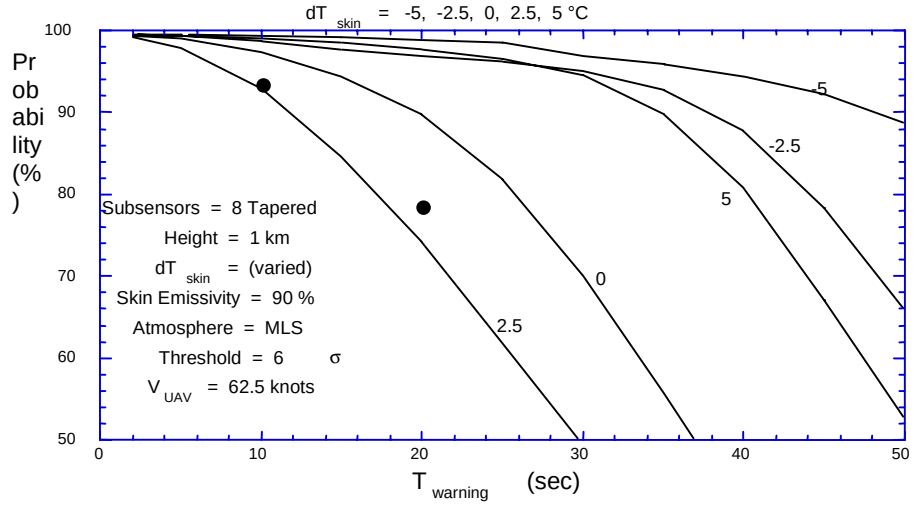

Figure 3: Altitude Dependence

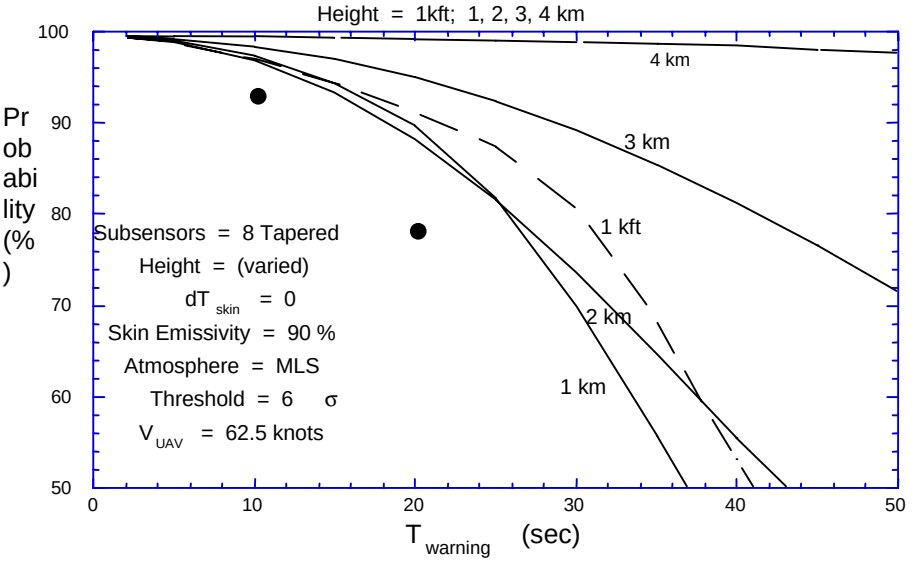

The types of detectors considered in this study are: (1) Uncooled, longwave, with low sensitivity and low cost, (2) Cooled PtSi, midwave, moderate sensitivity and cost, and (3) Cooled InSb, midwave, with high sensitivity and high cost. High quantum efficiency arrays must be cryogenically cooled. Individually they are much more sensitive than the uncooled long wave arrays, but the number of them that can be used on a UAV is limited. The weight of four dewars and closed cycle refrigerators is ten to twelve pounds, and the combined cost somewhere in the neighborhood of $160K for four PtSi and perhaps $400K for four InSb subsensors. And while sensitivity improves only as the square root of quantum efficiency, it improves as the third power of the number of subsensors. With uncooled technology, increasing the number of subsensors is both affordable and highly desirable. (See Section 3.2, Equation 8.)

Figure 4: Five Combinations of Arrays

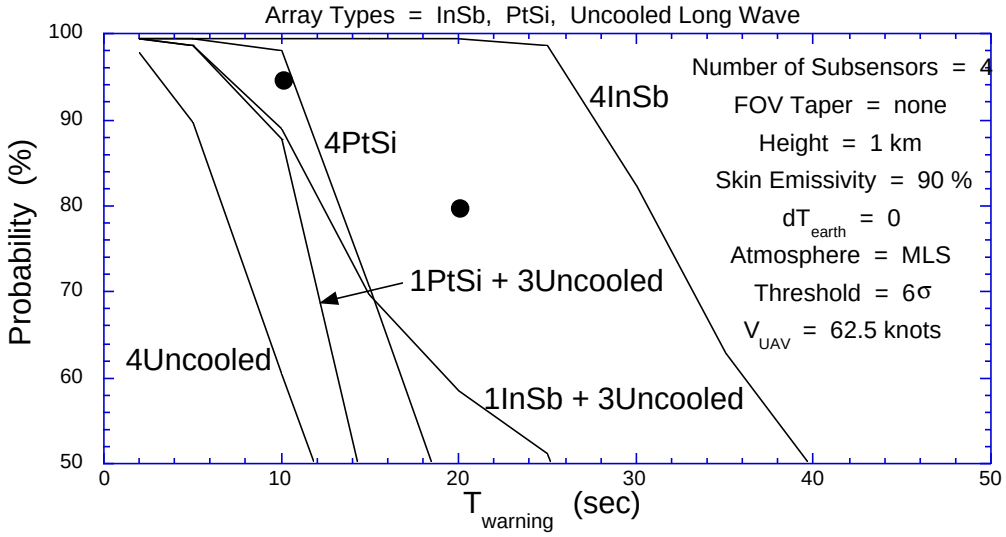

Figure 4 shows the performance of various four-subsensor combinations all with the same 90° field of view for every lens. A comparison of Figures 1 and 4 indicate that with about the same weight and far less cost, a PCAS system with twelve uncooled subsensors should match the performance of one with four high quantum efficiency arrays. Eight or ten uncooled subsensors should be sufficient depending on exactly how the warning time performance goal is defined.

2.0 Infrared Signature Measurement and Modeling:

A calibrated multiband infrared imaging sensor was used in the field to measure and record the contrast signatures of Cessna 172 and Piper Warrior aircraft viewed under a variety of flight conditions, view angles, backgrounds and ranges.[2] The infrared modeling computer code SPIRITS[3] was used to construct a model of the Cessna 172. This model was then fit to the field measurements in order to be able to extrapolate from the measured results and predict contrast signatures for generalized flight and viewing conditions. In the absence of solar heating, the measured results were well replicated by using 90% skin emissivity, setting the skin temperature of the aircraft to the local air temperature at flight altitude and then adding radiation from hot parts on the front and bottom of the air frame.

2.1 Cessna 172 and Piper Warrior Signature Measurement:

The multi-band IR imager contained both InSb and HgCdTe focal plane arrays sharing a common 6 inch aperture with 100 µRad resolution. Using synchronized filter wheels, the sensor collected imagery in the twelve spectral bands listed in Table 1 at 5 frames per waveband per sec. The output was radiometrically calibrated in the field against blackbody standard sources.

Table 1: Signature Measurements Spectral Bands

Midwave	Longwave
3.0 - 3.3	7.6 – 7.8
3.4 - 3.8	7.9 - 8.5
3.8 - 4.15	8.5 - 9.0
4.45 - 4.60	9.0 - 9.5
4.6 - 4.75	9.5 - 9.8
4.75 - 5.0	9.8 - 10.1

Four days of flights were conducted from the airports at Manassas and Luray in Virginia using the Cessna and Piper aircraft. Both aircraft have characteristic dimensions of 25 to 35 feet in length and wingspan with cross sectional areas of ~3.8 m^2 nose-on and ~8.8 m^2 in side view. The Cessna airframe has the main wing above the fuselage; in the Piper it is below. Small hot parts on these airframes are a pair of air intakes in the forward engine cowling and, especially, a short exhaust pipe extending below the cowling.

At Manassas the signatures were measured against a background of blue sky or scattered clouds at ranges of up to 5 nautical miles. At Luray the aircraft was flown between the sensor and the adjacent ridge mountain to achieve measurements in the presence of terrain clutter. The sensor was ground based.

2.2 SPIRITS Aircraft + Lowtran Background Modeling

To model these aircraft in SPIRITS, a facetized geometry was constructed from engineering drawings. Temperatures for "hot part" facets were taken from short range calibrated IR imagery described above. Good agreement between modeled and measured contrast was found from scene to scene of the recorded data, with the caveat that for the near-zero contrast cases the result depended sensitively on accurate estimate of the background.

The result is an ability to generate computer model images of the aircraft for generalized viewing geometry, for various background conditions and for the chosen spectral response bands of candidate warning sensors. Examples of modeled images are given in Figure 5. The hot parts are particularly noticeable. They can contribute significantly to contrast radiance in frontal aspects when the engine compartment and exhaust are in full view. However, hot parts constitute only a small part of the total viewed surface area of the aircraft, so they contribute only some 10–20% of the net absolute radiance. The dominant factors in establishing whether net contrast radiance is positive or negative are skin temperature and emissivity and background radiance.

Figure 5: SPIRITS MWIR Image of Cessna 172 against Lowtran MLS atmospheric background. The upward view shows net positive contrast, the downward view net negative contrast.

SPIRITS generates the integrated radiant output from all parts of the aircraft for the given view geometry and local air temperature, and Lowtran 7 is used to generate the radiance of the background path. The difference in these two is the net model contrast radiant intensity of the aircraft.

The absolute signature per unit area of the airframe before background subtraction would be $\approx 0.95 \times (10\ W / m^2\ \mu m\ Ster) \times 4.5\ \mu m = 43\ W / m^2\ Ster$ in the 8.0-12.5 μm band if the skin were at 80F and had 90% emissivity with half of its 10% reflectivity being of cold sky. Then if hot parts add 20% for front-side views the effective emissivity can, for estimation purposes, be approximated as $0.95 \times 1.2 \approx 115\%$. The corresponding radiance from gray bodies at the 1km altitude air temperature for each of the Lowtran model atmospheres is indicated in Figure 6 by the straight vertical lines. The curved lines are Lowtran-calculated path background radiance to sky or earth. An estimated contrast signature is then the difference between a curved and a straight line. Contrast signature is a small fraction of the absolute signature and in fact passes through zero at some elevation angle. It is the elevation position and sharpness of width of the contrast reversals that limit detectability of the aircraft. Accurate SPIRITS-based calculations of detection probability for the various atmospheres are given in Figure 7.

Figure 6: Lowtran Background Path Radiances
Versus Black Bodies at 1 km Altitude Air Temperatures

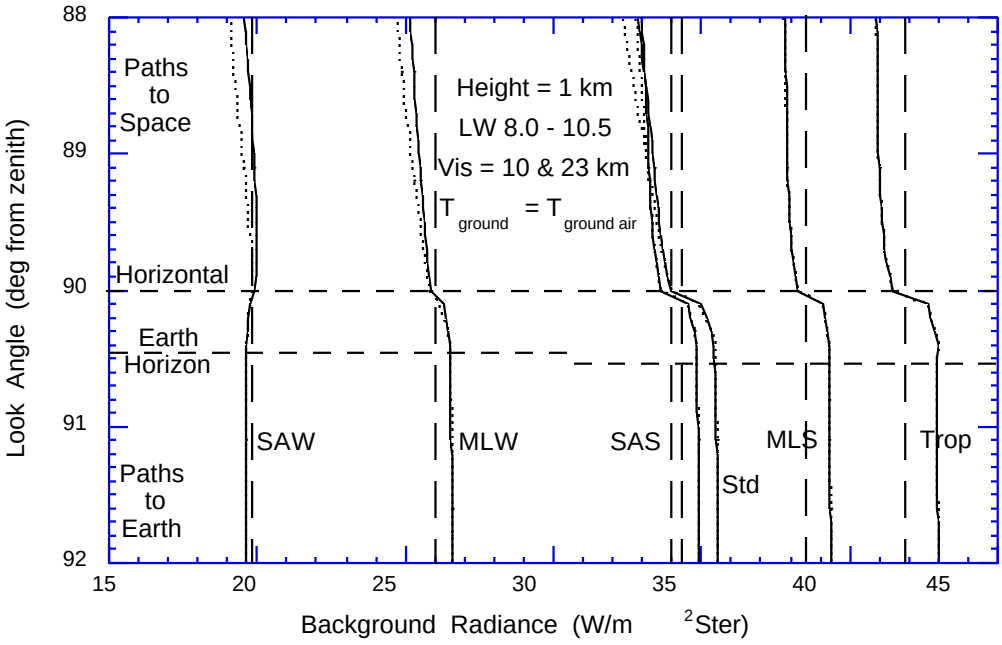

Figure 7: Effect Of Atmosphere and Lapse Rate

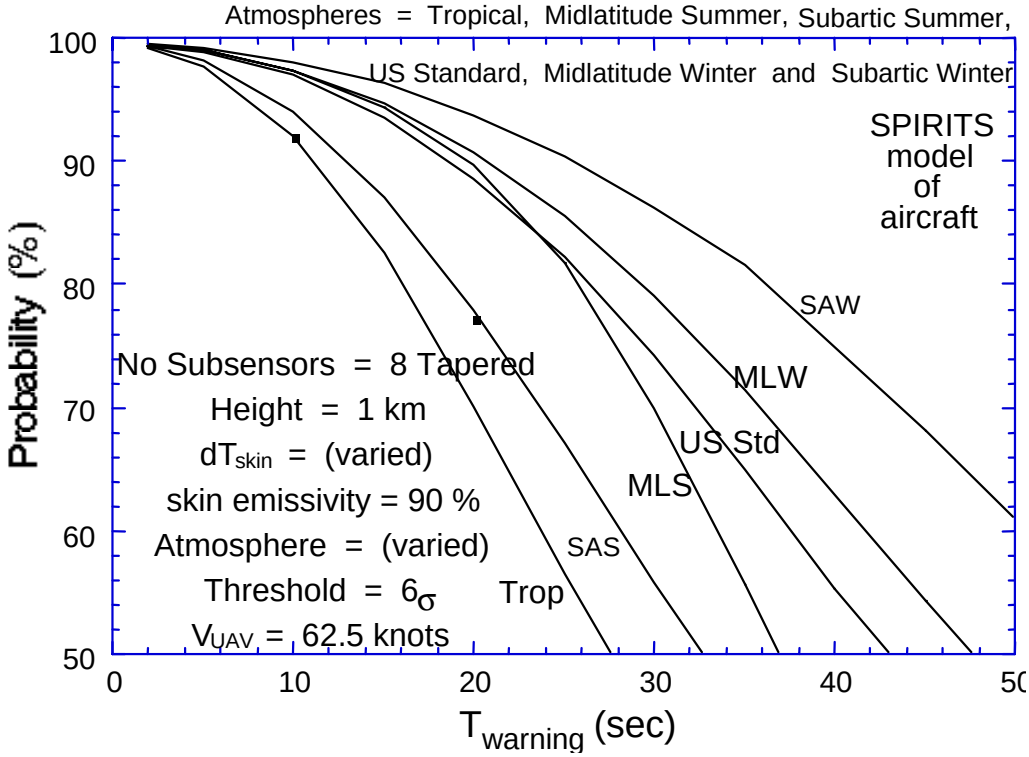

2.3 Contrast Reversals:

The contrast signature is a small fraction of absolute signature and passes through zero at some elevation angle as can be seen in Figure 6. The aircraft skin, set equal in temperature to that of the local air, will have a positive net heat radiation compared to the rest of the scene when the view to it is upward against cool sky. The relatively warm aircraft skin blocks part of the cool background radiation and replaces it with something brighter. The same would be true of a horizontal view if emissivity of the aircraft skin were 100%. Used in this report, though, is the SPIRITS model paint "AFGL-056"—approximately 90% emissivity in the long wave band with the associated 10% reflectivity being of sky or ground depending on the angle of each facet of surface area. Then horizontal-view contrast signature tends to be negative except for forward views in which hot parts contribute significantly. Eventually for downward views the aircraft contrast will always transition to negative with the standard Lowtran models that have warm ground. The angle between the horizontal and the horizon, neglecting ray bending, is $\arccos[1/(1+H/R_{earth})] \approx \sqrt{(2H/R_{earth})} = 1.00°$ at 1 km altitude.

Collision avoidance warning detection almost always involves viewing geometries that are nearly horizontal. This is because the non-maneuvering UAV and hazard aircraft must be at very nearly the same altitude if they are headed to a common collision point. As seen from the UAV, skin radiation from the aircraft and from the background are nearly the same, and the differenced contrast signature is small. Emissions from hot parts can then become significant, and the exact values of skin emissivity and temperature becomes important. Additional radiation from hot parts or solar heating shifts downward the viewing elevation angle at which the aircraft contrast signature transitions from positive to negative. Graphically, this a shift to the right of the solid gray body lines of Figure 6. The view factor of hot parts is a function of azimuth, and consequently, so too is the contrast reversal view angle. Effectively cool skin (as from low emissivity) tends to shift the contrast reversal elevation angles upward and shift the gray body lines of Figure 6 to the left. This movement up and down of the elevation of contrast reversals is shown in Table 2.

Table 2: Skin Temperature Variations of Cessna 172 SPIRITS-Lowtran contrast signature in the long-wave 8.0-12.5 μm band. Az is the azimuth position of the observer relative to the hazard aircraft, with 0° being nose-on and 180° being a view from behind. El is the elevation of the observer's look direction from horizontal; positive values mean looking up. The three sub-tables are for dT_{skin} = +2.5C, 0C and -2.5C relative to the 61.7F Lowtran Midlatitude Summer local air temperature at 1 km. Skin emissivity is approximately 90%.

Az0	15	30	45	60	75	90	105	120	135	150	165	180	El
12.16	11.79	17.87	20.97	22.50	21.28	20.90	17.88	8.56	-0.12	-7.34	-15.76	-21.14	2
7.91	5.35	9.58	11.29	13.05	12.69	12.97	6.04	-4.11	-11.20	-16.63	-23.43	-27.45	1
4.40	1.00	5.63	6.48	6.55	6.06	5.64	-4.66	-13.27	-17.13	-21.12	-25.15	-28.61	0
-4.93	-6.15	-8.38	-9.75	-11.85	-13.26	-17.80	-27.36	-33.29	-34.07	-34.29	-35.12	-34.38	-1
-3.80	-4.99	-7.05	-9.10	-11.25	-15.29	-21.90	-29.44	-33.59	-33.59	-34.04	-33.58	-34.56	-2
8.86	7.29	11.07	12.47	12.70	10.98	10.80	7.68	-0.93	-8.42	-14.04	-20.26	-23.84	2
4.61	0.75	2.78	2.79	3.25	2.49	2.87	-4.15	-13.71	-19.60	-23.43	-28.13	-30.32	1
1.10	-3.69	-1.16	-2.11	-3.34	-4.24	-4.45	-14.86	-22.97	-25.83	-28.22	-30.15	-31.72	0
-8.33	-10.85	-15.18	-18.35	-21.75	-23.56	-27.80	-37.76	-43.29	-43.07	-41.69	-40.42	-37.88	-1
-7.10	-9.79	-13.95	-17.70	-21.15	-25.59	-31.80	-39.84	-43.79	-42.79	-41.74	-39.18	-38.46	-2

5.46	2.49	4.07	3.87	2.80	0.68	0.60	-2.51	-10.53	-16.62	-20.54	-24.66	-26.34	2
1.11	-4.04	-4.11	-5.80	-6.74	-7.80	-7.22	-14.35	-23.31	-28.00	-30.13	-32.73	-33.11	1
-2.39	-8.59	-8.26	-10.91	-13.24	-14.64	-14.55	-25.16	-32.77	-34.33	-35.22	-35.05	-34.75	0
-12.03	-15.75	-22.28	-27.05	-31.75	-33.86	-37.80	-48.06	-53.19	-51.87	-48.99	-45.62	-41.28	-1
-10.60	-14.79	-21.15	-26.50	-31.15	-35.89	-41.80	-50.24	-53.89	-51.89	-49.44	-44.78	-42.26	-2

3.0 Candidate Subsensors, Their Sensitivity And Use:

Four candidate-technology subsensors were considered for PCAS performance analysis. These are indicated in Table 3 with estimated sensitivities and in-band atmospheric transmission. The camera costs listed are for the standard camcorder type of packages now available for each of these devices. The NEI values listed are for 640 detectors looking into a specialized lens with 90° field of view. Further, it was assumed when estimating NEI that the blur image of an unresolved, distant "point" source is equally split between two detectors. A full discussion of NEI is given here only for the most important technology class–uncooled, longwave, microbolometer and ferroelectric arrays.[4,5]

Table 3: Characteristics Of Candidate Subsensors. These NEI's assume 640 detectors viewing a 90° field of view and an equal split of point blur image between two detectors.

Device	Camera $K	Spectral Band µm	NEI pW/cm^2	Extinction /km	T_{1km} %
InSb	120	4.5-4.8	.0554	.105	90
PtSi	40	3.35-3.75	.177	.288	75
PtSi	40	3.75-4.15	.350	.163	85
Uncooled	12	8.0-12.5	84.8	.051	95

3.1 Uncooled Long-Wave Subsensors, The Basic Design:

A major design criterion here is that total weight should be kept to less than 20 pounds. Optics can constitute the major part of this load, since detector arrays are much lighter than lenses. Unlike high-performance cryogenic arrays with their several-pound closed-cycle refrigerators and dewars, uncooled long-wave arrays in their thermal holders weigh no more than three ounces. Consequently, there can be many of them without severe weight penalty. PCAS involves a 360° search in azimuth but only a narrow search in elevation. This means that of the 640x480 detectors in a commercial array, only some 80 contiguous rows need to be defect-free and supported by electronic processor. The arrays can be inexpensive production line rejects, and approximately six of them can be operated with one electronics package. Electronics and housing for the sensor might weigh five pounds. The rest of the 20 pounds weight can be devoted to optics (lenses) within size, cost and weight restraints.

The above discussion is oriented toward the staring approach. The scanning approach is less attractive from several points of view. Scanning systems are preferred when high resolution (~100 µrad) is needed for spatial filter clutter rejection. However, typical PCAS look down angles are only half a degree; for example, an hazard aircraft climbing from the side at 100 ft/min [arctan (100 knots/100 ft/min) ≈ 0.6°], or about the same depression angle as the flat-ground horizon from three thousand feet [$\arccos\{1/(1+H/R_{earth})\} \approx 1°$]. Except for looking horizontally at a steep mountain side, the ground and cloud scenes that will be viewed by PCAS are at such a small elevation angles that there is little discernible spatial structure. Consequently there is no compelling need for high resolution. Furthermore, the scanner approach is cumbersome both mechanically and in track processing.

The system considered here is a composite sensor comprised of a cluster of small subsensors. It is assumed that each contains a commercially available uncooled focal plane array of width 640x25 µm = 16 mm and that these subsensors together span the 360° azimuth. If there are N subsensors, the focal length of each must be

$$f = \frac{8\ \text{mm}}{\tan(180°/N)} \qquad (1)$$

=	8.0 mm,	N = 4,	FOV = 90°,
=	13.6 mm,	N = 6,	FOV = 60°,
=	19.3 mm,	N = 8,	FOV = 45°,
=	24.6 mm,	N = 10,	FOV = 36°,
=	29.9 mm,	N = 12,	FOV = 30°,
=	45.4 mm,	N = 18,	FOV = 20°,

The 30 mm, 30° FOV lens with F/0.8 would probably weigh less than a pound, or less than ten pounds for a dozen of them.

A strong candidate for the PCAS system is a bundle or pod of eight staring subsensors. With this choice the PCAS subsensors are nearly identical to the imager in an Army development program for a Driver's Vision Enhancer to be deployed on Bradley vehicles and M1 tanks. A stressing goal of this Army program is low cost, and the present generation prototype design is estimated in production at $15-20K complete with turret, flat panel display and operator controls. The imager uses an uncooled focal plane array with an F/1, 40° width, 50° diagonal field-of-view lens. An entire PCAS cluster pod using sector readout of reject detector arrays and without the display, turret and tank ruggedization should cost approximately the same as this Army system.

The N = 8, 45° field of view PCAS lens is very similar to that of the Army program. With 25 µm pitch between detectors, the instantaneous field of view varies from $\phi = 1.10$ mRad at the center to 1.29 mRad at the edge of the array.

3.2 Uncooled Long-Wave NEI:

The MRΔT sensitivity of uncooled, long-wave focal plane arrays with F/1 optics is approximately 50 mK.[6] The Texas Instruments ferroelectric technology is the furthest along in packaging and has 320x240–array products with MRΔT of 60-80 mK. With the microbolometer technology being pursued by SBRC, Amber/Rockwell and Lockheed Martin, single-unit 320x240 devices have been produced with MR$\Delta T \approx 40$ mK. Development work being funded by ARPA and Army is for the larger 640x480 array size with no loss in sensitivity.

Current array sizes are 320x240 with detector pitch of 50 µm. This chip is already at the maximum practical size limit of one inch (diagonal), so the development objective is to reduce detector size by a factor of two in order to achieve a 640x480 array size. The task is difficult in many respects. Noise is approximately independent of detector size, but signal drops in proportion to detector area. The microbolometer fill factor is 50-60% now and drops to some 25% with the 25µm pitch. Similarly the ferroelectric approach has comparable thermal crosstalk MTF problems that are compounded by the smaller size. Signal responsivity to temperature change must to be improved significantly without a nonuniformity penalty if MRΔT is to be maintained. It is anticipated that NEΔT may initially degrade during the coming year when the initial 640x480 arrays are produced and then return to or improve

compared to the 50 mK of today's 320x240 arrays in another year or two. These NEΔT values are stated for F/1. Current industry reports of progress are better than anticipated.

The sensitivity performance specification needed for PCAS modeling calculations is NEI rather than NEΔT. For a given sensor with fixed F/# and detector pitch w_{det}, the relationship between these is

$$NEI(F/\#, \phi) = 2\ NE\Delta T\ (F/\#)\ \frac{dW}{dT}\ \phi^2, \qquad (2)$$

where dW/dT is the differential radiance of the scene, ϕ^2 is the solid angle in steradians of a pixel instantaneous field of view and the factor of 2 accounts for the possibility of the unresolved source being divided between two or more pixels. In principle a factor as large as 4 should be used if warning probabilities near 100% are to be calculated, but for 30 Hz frame rates there will be a sufficient number of threshold crossings with just the factor of 2.

With a small-angle approximation,

$$\phi \approx FOV/640 \qquad (3)$$

dW/dT is given in Table 4 for various temperatures and spectral bands. The value that will be used here is

$$dW/dT \approx 7x10^{-5}\ Watts/cm^2Ster°C. \qquad (4)$$

Table 4: Blackbody Differential Contrast Radiance

Δλ = 8.0-12.5 μm		T = 80 F	
T (F)	$W/m^2Ster°C$	Δλ (μm)	$W/m^2Ster°C$
100	.781	7.5-13.5	.900
80	.704	8.0-12.5	.704
60	.629	8.0-12.0	.645
40	.555		

Note that NEΔT depends only on F/# and not on φ, and specifically that since these arrays are internal noise rather than BLIP limited,

$$NE\Delta T \propto (F/\#)^2. \qquad (5)$$

For purposes of modeling it is assumed here that for practicably achievable optical designs the F/# changes with field of view according to

$$F/\# \approx \sqrt{\frac{FOV}{40°}}\ , \qquad 25° \bullet FOV \bullet 130° \qquad (6)$$

$$\approx 1.8\ , \qquad 130° < FOV$$

$$\approx 0.8\ , \qquad FOV < 25°\ .$$

Equation 2 becomes

$$NEI(FOV) = 2\ NE\Delta T_{F/\#=1}\ (F/\#)^2\ \frac{dW}{dT}\ \left(\frac{FOV}{640}\right)^2, \qquad (7)$$

which for 40° FOV and hence F/1 is $2x0.05x7x10^{-5}x1.09^2x10^{-6} = 8.32\ pW/cm^2$. More generally, Equation 2 becomes

$$NEI(FOV) = 8.32\ pW/cm^2 \left(\frac{FOV}{40°}\right)^2, \qquad 25° \bullet FOV \bullet 130°$$

$$= 27.0\ pW/cm^2 \left(\frac{FOV}{40°}\right)^2, \qquad 130° < FOV$$

$$= 5.32\ pW/cm^2 \left(\frac{FOV}{40°}\right)^2, \qquad FOV < 25°$$

If PCAS were comprised of identical uncooled subsensors, each with the same FOV, the model sensitivity would be

Table 5: Model Uncooled NEI For Equal FOV Subsensors

N	FOV (deg)	NEI (pW/cm^2)
4	90	94.8
6	60	28.0
8	45	11.8
10	36	6.06
12	30	8.32
18	20	1.33

Use of equal focal lengths for all lenses is not optimal. Greater detection ranges and sensitivities are needed in forward, nose-on geometries than in the rearward, tail-chase directions. Subsensor focal length should be longer, and field of view narrower, in the forward direction. The focal lengths given in Table 6 are found in the present modeling to give optimal warning time performance for an eight-subsensor PCAS cluster of 640 element long arrays. The longest 35 mm focal length lens is pointed straight forward in order to achieve the greatest sensitivity where it is needed the most. Then 27 mm lenses are positioned on either side of this. A single 10 mm lens subsensor points directly to the rear.

Table 6: Model NEI Performance For Uncooled PCAS With Eight Subsensors Using 640-Long Detector Arrays With 50 mK F/1 NEΔT

FOV (deg)	f (mm)	F/#	ϕ (mRad)	NEI (pW/cm^2)
26	34.7	.806	0.72	2.3
33	27.0	.908	0.92	4.8
41	21.4	1.01	1.2	9.0
55	15.4	1.17	1.6	22
76	10.2	1.38	2.5	57

Performance always improves if a still larger number of subsensors is used. Weight increases as well, partly because of the increased number of subsensors but also because of increasing focal lengths and improved F/#'s. Table 7 shows the field of view and focal length allocations for several cases and also gives a rough estimate of total lens weight. In the case of eight subsensors the heaviest F/0.8 35 mm lens should probably weigh less than a pound. With ten subsensors there would be three F/0.8 lenses weighing perhaps a pound or more, the 40 mm and the two 35 mm lenses, but as complemented with the shorter focal length lenses the total lens weight might still be acceptable. The weight of a twelve-subsensor cluster is questionable for a light-weight UAV payload.

Table 7: Tapered Fields of View Versus Number Of Subsensors
(Fields of view in degrees, Focal length's in mm, Weight in pounds.)

Subsensors	4	6	8	10	12
FOV 1	66°/12	42°/21	26°/35	22°/41	19°/48
FOV 2	77°/10	49°/18	33°/27	24°/38	20°/45
FOV 3	140°/2.9	61°/14	41°/21	30°/30	22°/41
FOV 4		98°/7	55°/15	36°/25	26°/35
FOV 5			76°/10	46°/19	31.5°/28
FOV 6				66°/12	42°/21
FOV 7					58°/14
≈Σ Lens Weights	1-2	2-3	4-6	6-7	10-12

4.0 Method Of Calculation for $P(T_{warning})$:

UAV's flying below cloud level will usually avoid airports. This means that they are not likely to encounter twin engine or high performance aircraft, which generally fly at higher altitudes. Rather, it is the smaller, single-engine class of aircraft that is most likely to pose a concern of mid-air collisions for the UAV. These aircraft are referred to in this report as "hazard aircraft" when they are on a collision course with the UAV.

It is assumed in the absence of warning that neither the UAV nor the hazard aircraft are making intentional maneuvers and that their flight paths can be approximated by straight lines during the last several tens of seconds before impending collision. It is further assumed that the UAV flies straight and level with velocity $V_{UAV,}$ and that relative to its direction in the horizontal plane the hazard aircraft flies at velocity $V_{hazard\ horiz}$ ingressing randomly from any angle Ω toward the intercept point. In the elevation direction all wander of the two aircraft is represented in a single small-value parameter, $V_{hazard\,climb\,rate}$, that is a random variable representative of non-instrumented aircraft flight characteristics. Collision is generally defined as a near miss by distance $|Z_{offset}| < 30$ ft in the elevation direction. Then at a time $T_{to\,go}$ before the impending collision the slant range between the two aircraft is a function of all these parameters:

$$R_{separation} = F_1(T_{to\,go}, V_{UAV}, V_{hazard\,horiz}, \Omega, V_{hazard\,climb\,rate}, Z_{offset}) \qquad (8)$$

The achievable range at which the sensor on the UAV can detect the presence of the hazard aircraft is a function of atmospheric extinction α, sensor NEI(FOV, $\Delta\lambda$, …) and hazard aircraft contrast signature CSig(θ's, Ø's, H, …), which itself is a complicated function of viewing geometry, altitude, skin emissivity, solar heating, atmospheric lapse rate and ground or cloud background:

$$R_{detect} = F_2(\alpha, NEI, CSig(\theta's, Ø's, H, \ldots)) \qquad (9)$$

Finally, by comparing these two ranges, a "yes–no" function can be defined as:

$$\begin{aligned} Y(T_{to\,go}, \ldots) &= 1, \quad R_{detect} \bullet R_{separation} \\ &= 0, \quad R_{detect} < R_{separation} \end{aligned} \qquad (10)$$

A considerable simplification of these equations can be realized by setting $Z_{offset} = 0$. In this case, the angles between the two aircraft depend only on Ω, $V_{hazard\,horiz}/V_{UAV}$ and $V_{hazard\,climb\,rate}/V_{UAV}$ and not on $T_{to\,go}$. Equation 8 reduces to a dependence on only these same three parameters,

$$\left[\frac{R_{separation}}{T_{to\,go}\,V_{UAV}}\right]_{Z_{offset}=0} = F_1'\left(\Omega, \frac{V_{hazard\,climb\,rate}}{V_{UAV}}\right). \qquad (11)$$

A similar simplification is effected for Eq. (9) because the geometry of the collision is independent of the time variable.

In both the full and simplified form of Eqs. 8 and 9, the three parameters Ω, $V_{hazard\,horiz}/V_{UAV}$ and $V_{hazard\,climb\,rate}/V_{UAV}$ are treated as random variables scanning what will be referred to here as "equal probability space." The "yes–no" function Y is then averaged in this probability space, within bounds characteristic of hazard aircraft flight characteristics, in order to achieve the warning success probability:

$$P(T_{warning}, \ldots) \equiv$$

$$.90\ \langle\langle Y(\Omega, V_{hazard}, V_{climb}) w(V_{hazard}) w(V_{climb})\rangle\rangle_{\substack{0^\circ \bullet \Omega \bullet 180^\circ \\ 80\,\text{knots} \bullet V_{hazard\,horiz} \bullet 140\,\text{knots} \\ -150\,\text{ft/min} \bullet V_{hazard\,climb\,rate} \bullet +150\,\text{ft/min}}}$$

$$+.05\ \langle\langle Y(\Omega, V_{hazard} = 80\,\text{knots}, V_{climb} = +500\,\text{ft/min})\rangle\rangle_{0^\circ \bullet \Omega \bullet 180^\circ}$$

$$+.05\ \langle\langle Y(\Omega, V_{hazard} = 140\,\text{knots}, V_{climb} = -500\,\text{ft/min})\rangle\rangle_{0^\circ \bullet \Omega \bullet 180^\circ}, \qquad (12)$$

Here $T_{warning} \equiv T_{to\,go}$. The numerical implementation of the averaging operations uses step sizes of $\Delta\Omega = 0.5°$, $\Delta V_{hazard} = 5$ knots and $\Delta V_{hazard\,ascent\,rate} = 1.5$ ft/min, and the weighting functions $w(V_{hazard})$ and $w(V_{climb})$ are included to assign reduced probability of occurrence to the higher magnitudes of hazard aircraft speeds and climb rate. The first term is for hazard aircraft flying nominally, but not strictly, level as discussed. The last two terms add rare possibilities that the hazard aircraft could be rapidly climbing or descending, as in the vicinity of an airport. Sensitivity analysis shows that $P(T_{warning}, \ldots)$ as defined is virtually independent of Z_{offset}, so this parameter can be ignored for the purpose of establishing PCAS feasibility. A similar remark concerns the parameter V_{UAV} with the understanding that the ratio of velocities, V_{hazard} / V_{UAV} is an important parameter.

In picture form, the averaging operations in Equation 12 are equivalent to determining the relative abundance of white versus black in Figure 8. The black bands show regions in probability space where Y = "no" near hazard aircraft signature contrast reversals, and the shades of gray represent the weighting functions $w(V_{hazard\,horiz})$ and $w(V_{hazard\,climb\,rate})$. The jagged-edge stepping in the black bands is caused by field of view tapering and the associated NEI stepping in Ω between subsensors. Warning success probability calculations are essentially just the task of figuring out probabilistically where hazard aircraft contrast reversals occur as a function of the three probability space geometry parameters.

Figure 8: Equal Probability Space Plots of the averaging in Equation 12. Y = ±1 is depicted as light or dark and is shown as a function of three parameters. Ω = 1 to 180° is from left to right. The four main bars in each figure are for nominally level hazard aircraft flight with $V_{\text{hazard horiz}}$ = 80, 100, 120 and 140 knots. UAV look-up or look-down angle to the hazard aircraft is represented within a given bar with $V_{\text{hazard climb rate}}$ varying from -150 to +150 ft/min. The two thin bars, nearly all Y = +1, across the bottom depict the fixed-climb-rate, near-airport cases. The black bands are regions of hazard aircraft contrast signature reversal. Contrast is positive above a black bands and negative (but detectable) below. Figure a was generated during calculations for the 20 sec point on the 8T curve of Figure 1. Skin temperature has been raised 2.5 C in the right-hand figure, thereby lowering the UAV view angles to hazard aircraft contrast reversals.

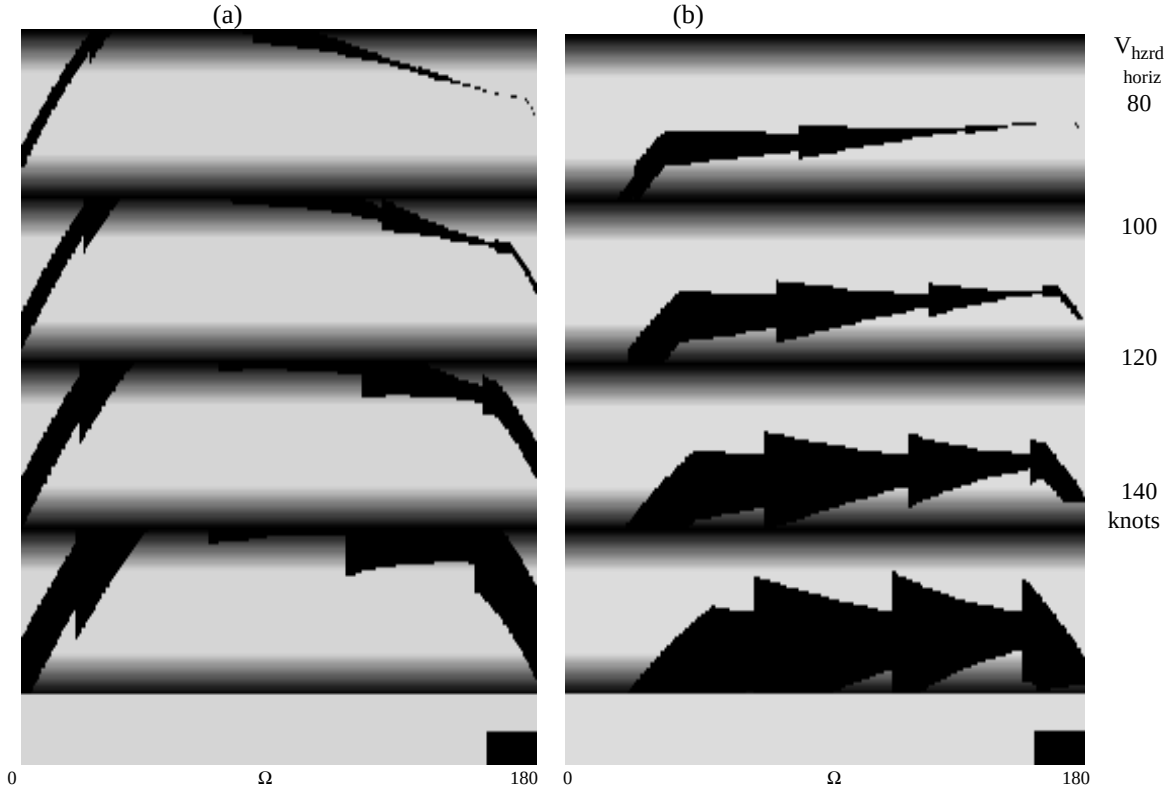

Figure 9: Insensitivity on UAV Velocity

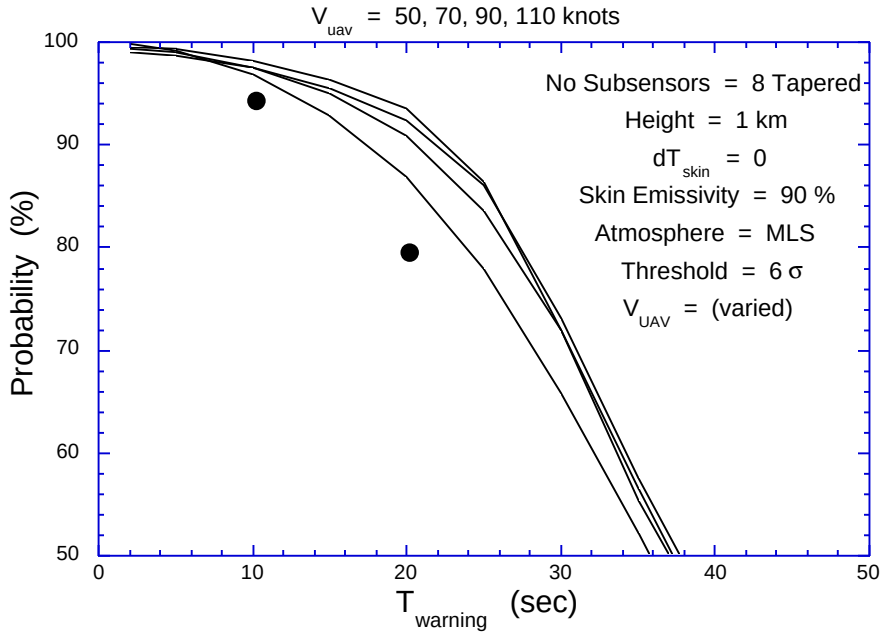

Figure 10: Moderate Insensitivity on Z Offset

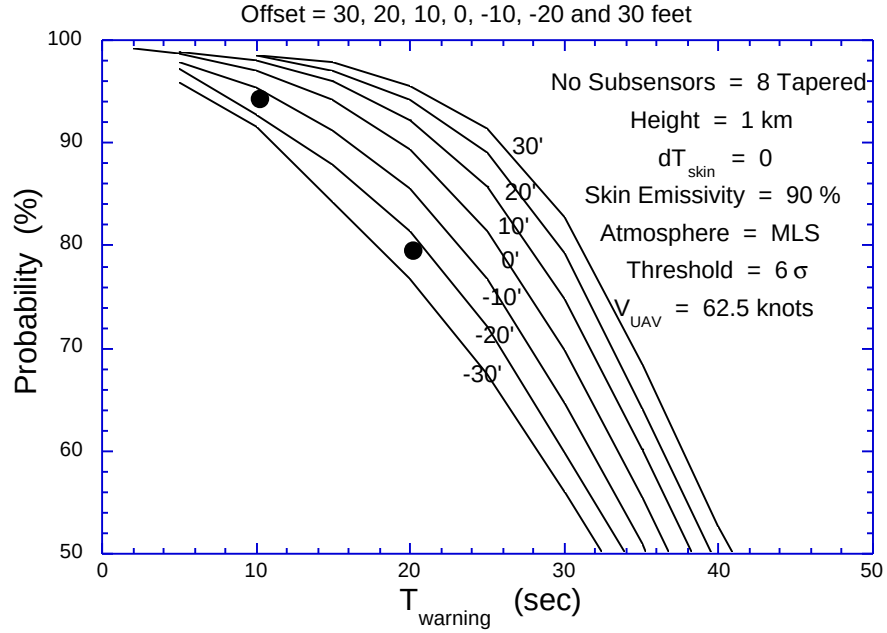

Figures 9 and 10 show the insensitivity of $P(T_{warning})$ to V_{UAV} and Z_{offset}. It is sufficient to use $Z_{offset} = 0$, because averaging over this parameter would give very nearly the same result for the probability of warning success.

The bound of $|V_{hazard\,climb\,rate}| \bullet 150$ ft/min for nominally level flight is based on measured data taken during in a Cessna aircraft during smooth to slightly bumpy air conditions. It was a non-instrumented flight with the pilot paying a normal degree of attention to the cockpit altimeter.

Figure 11: Four altitude drift records during Cessna flight with manual pilot control during smooth to light chop conditions.
The dashed line is for reference.

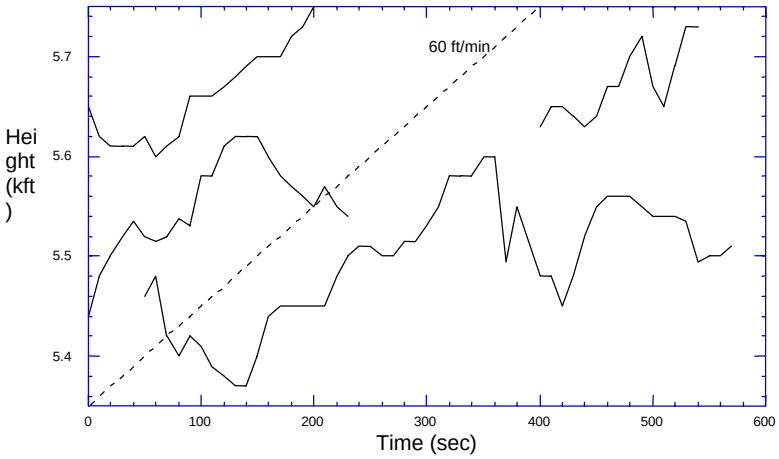

Figure 12: Horizontal Plane of Collision Geometry. The hazard aircraft comes with equal probability from any angle Ω toward the intercept point X. Its speed ranges from 0.8 to 1.4 times that of the UAV.

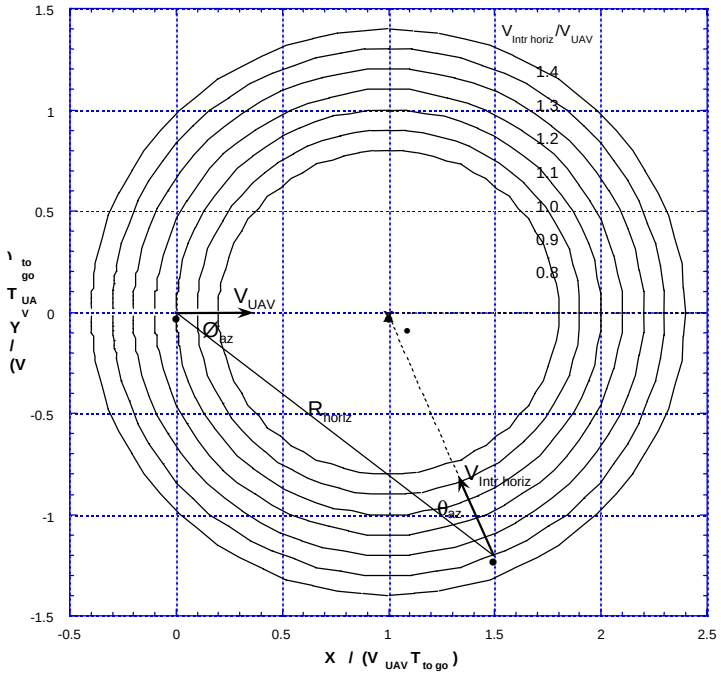

The variables Ω and $V_{hazard\,horiz}$ are depicted in real collision space in Figure 12. This is a vertical view looking down on a horizontal plane showing only horizontal components. The UAV is flying from the left at velocity V_{UAV} = 62.5 knots toward the impending collision point marked by an X. The hazard aircraft flying at velocity $V_{hazard\,horiz}$ = 80 to 140 knots is approaching the same intercept point but from anywhere on a circle of radius $V_{hazard\,horiz}T_{to\,go}$. Ω = 0° is the nose-on, long-range case.

$\Omega \approx 180°$ is the short-range tail-chase. The computational code has been written for generality, but the algebraically subtle $V_{\text{hazard horiz}} < V_{UAV}$ cases shown in the figure never actually occur in Equation 12 .

Climb or descent of the hazard aircraft introduces the elevation direction dimension not shown in Figure 12. The view angles between the aircraft then have two components, and these will be written as

$$\begin{aligned} \text{ø}_{az}, \text{ø}_{el} &\equiv \text{UAV polar view angles} \\ \theta_{az}, \theta_{el} &\equiv \text{hazard polar view angles}. \end{aligned} \tag{13}$$

$V_{\text{hazard climb rate}}$ is small compared to $V_{\text{hazard horiz}}$, so the distances involved in the elevation direction above or below the plane of Figure 12 are not large. There is a limited possibility, though, that the elevation angles ø_{el} and θ_{el} could approach ±90°. This would happen near a tail chase if the hazard aircraft and UAV speeds were nearly the same, but Equation 12 always uses $V_{\text{hazard horiz}} > V_{UAV}$. Even for faster UAV's as in Figure 9, the statistical occurrence of large ø_{el} and θ_{el} is negligible. A computational bound always placed on Equation 12 is Y = 0 or "no" for $|\text{ø}_{el}| > 10°$. This is found to never affect numerical results.

4.1 Equations:

The normalized parameters of Equation 11 are defined as:

$$\begin{aligned} U_{\text{horiz}} &\equiv V_{\text{hazard horiz}} / V_{UAV}, \\ U_{el} &\equiv (V_{\text{hazard climb rate}} + Z_{\text{offset}} / T_{\text{to go}}) / V_{UAV}, \\ \rho_{\text{horiz}} &\equiv R_{\text{horiz}} / V_{UAV} T_{\text{to go}}. \end{aligned} \tag{14}$$

Formulas for calculations are then:

$$\rho_{\text{horiz}} = \sqrt{1 + U_{\text{horiz}}^2 + 2\, U_{\text{horiz}} \cos\Omega}\ , \tag{15a}$$

$$\theta_{\text{az off hazard}} = \arcsin\left(\frac{\sin\Omega}{r_{\text{horiz}}}\right), \qquad U_{\text{horiz}} > 1 \tag{15b}$$

$$= \arcsin\left(\frac{\sin\Omega}{r_{\text{horiz}}}\right), \qquad \Omega < \arccos(-U_{\text{horiz}}),$$

$$= 180° - \arcsin\left(\frac{\sin\Omega}{r_{\text{horiz}}}\right), \quad \Omega > \arccos(-U_{\text{horiz}}), \tag{15c}$$

$$\theta_{\text{el off hazard}} = -\arctan\left(\frac{U_{el}}{\rho_{\text{horiz}}}\right), \tag{15d}$$

$$\text{ø}_{\text{az off UAV}} = \Omega - \theta_{\text{az off hazard}}\ , \tag{15e}$$

$$\text{ø}_{\text{el off UAV}} = \arctan\left(\frac{U_{el}}{\rho_{\text{horiz}}}\right), \tag{15f}$$

$$R_{\text{separation}} = V_{UAV}\, T_{\text{to go}} \sqrt{\rho_{\text{horiz}}^2 + U_{el}^2}\ . \tag{15g}$$

The redundant subscripts are used here to emphasize the distinction between ø's and θ's. Three-parameter «» averaging in Equation 12 over Ω, $V_{\text{hazard horiz}}$ and $V_{\text{hazard climb rate}}$ is incremented in computer code in three loops. A fourth loop is required in order to achieve one of the curves shown for $P(T_{\text{warning}})$. As discussed above, some simplification of this process is possible when $Z_{\text{offset}} = 0$.

Detection ranges that the sensor can achieve are calculated using converging iteration of the formula

$$R_{\text{detect}} = \sqrt{\frac{| Q(\theta_{az}, \theta_{el}, T_{skin}, \Delta\lambda, \ldots) | e^{-\alpha R_{\text{detect}}}}{\varepsilon \, \text{NEI}(\text{FOV}\{\Omega\}, \Delta\lambda, \ldots)}} \qquad (16)$$

where Q is the contrast infrared signature of the hazard aircraft viewed against its background, α is the extinction coefficient of the atmosphere, NEI is the sensitivity of a given subsensor on the UAV, and a threshold exceedance factor of ε = 6 is used. This somewhat conservative value is chosen to be certain that a track processor, which would be required to handle detections from the front end which has been described here, would not be swamped with false detections.[7]

5.0 Conclusion

A PCAS based on a minimum of 8 uncooled LWIR staring sensors appears to be feasible. The system, exclusive of the real-time processor, could weigh as little as 20 pounds and cost as little as $100,000. The system would provide 20 seconds of collision warning with 80% confidence and at least 10 seconds of warning with 95% confidence. Due its passive character, the system would not compromise UAV mission effectiveness.

6.0 Acknowledgments

The authors wish to acknowledge the support of J.E. Miller of NVEOL for providing information on uncooled detector technology. The support of USSOUTHCOM is gratefully acknowledged.

7.0 References

1. This information may be found on the following World Wide Web page: http://www.acq.osd.mil/daro/homepage/uav96/content.html

2. E. J. Stone et. al., "Measured Infrared Signatures of Light Aircraft",. Proceedings, IRIS Specialty Group on Targets, Backgrounds and Discrimination, ERIM 440000-30-X, p. 385 (1997).

3. J. Conant et al., "SPIRITS - a Model for Spectral Infrared Imaging of Targets and Scenes," Proceedings, Meeting of the IRIS Specialty Group on Targets, Backgrounds, and Discrimination, ERIM document 180400-1-X, vol. 1, p. 129 (1985)

4. S. Campana, Editor, *Passive Electro-Optical Systems* , Vol. 5 of *The Infrared & Electro-Optical Systems Handbook*, (SPIE Optical Engineering Press, Bellingham, WA. 1993).

5. C. Webb and M. Norton, "Measurement Review of Infrared Staring Systems", Proc. NATO-IRIS Vol. 41, No. 1, p. 317 (1996)

6. J.E. Miller, "Uncooled Handheld Infrared Surveillance Camera", Office of National Drug Control Policy, International Technology Symposium, October 1995

7. A. Wahlen, *Detection of Signals in Random Noise* , Chapt. 5, (Academic Press: San Diego, 1971)